ROYAL SOCIETY OF CHEMISTRY

PAPER

Check for updates

A critical revelation of lithium ferromanganese phosphate (LMFP) performance in a Mn-rich cathode for Li-ion batteries using Fe equivalents to occupy a Mn site†

Ruifen Yang,[ab] Longjiao Chang, ✱[ab] Shaohua Luo, ✱[cd] Xiaolong Bi,[ab] Wei Yang,[ab] Kedi Cai,[ef] Anlu Wei[ab] and Zenglei Hou[ab]

The modification of a polyanionic positive electrode material $LiMnPO_4$ by transition metal doping was experimentally studied on the basis of carbon coating in order to address the drawbacks of low electronic conductivity and charge−discharge performance. A hydrothermal procedure was successfully used to create a $Li(Mn_{1-x}Fe_x)PO_4/C$ (x = 0, 1/24, 1/12, 1/8, and 1/4) cathode material, and its performance was evaluated. After comparing the material's electrochemical performance at different doping concentrations, the ideal Fe content was found to be x = 1/4. The $Li(Mn_{1-x}Fe_x)PO_4/C$ sample exhibits excellent electrochemical performance, discharge ability of 141.6 mA h g^{-1}, 100 cycles at 1C rate, capacity retention ratio of 97.88%, and the best kinetic characteristics. First principles calculations showed that the $Li(Mn_{1-x}Fe_x)PO_4/C$ material has the smallest band gap, and the total state density is closest to the Fermi level; thus, more electrons can be used to transition to the conduction band, which is the reason for its excellent discharge ability. The introduction of Fe reduces the ELF function value near the original Mn position and decreases electron localization and the diffusion energy barrier, which is very conducive to electron movement and improves the diffusion kinetics of lithium ions in a doping system.

1 Introduction

At a time when oil and other conventional energy sources are increasingly scarce around the world, there is an exigent need for the effective development and use of sustainable energy, such as solar, wind and tidal energy.[1] Nevertheless, these new sources of energy are unstable and constant; thus, they need to be converted into electricity before they can be exported, which has motivated research on rechargeable batteries. Lithium-ion batteries (LIBs) have become the dominant technology in the field of man-carried electronic equipment and electromobiles

[a] School of Chemical and Material Engineering, Bohai University, Jinzhou, 121013, Liaoning, China. E-mail: jsz337@sina.com

[b] Liaoning Key Laboratory of Engineering Technology Research Center of Silicon Materials, Jinzhou, 121013, Liaoning, China

[c] Key Laboratory of Dielectric and Electrolyte Functional Material Hebei Province, Qinhuangdao, 066004, Hebei, China. E-mail: tianyanglsh@163.com

[d] School of Resources and Materials, Northeastern University at Qinhuangdao, Qinhuangdao, 066004, Hebei, China

[e] College of Chemistry and Materials Engineering, Bohai University, Jinzhou 121000, China

[f] Liaoning Engineering Technology Research Center of Supercapacitor, Bohai University, Jinzhou, 121013, China

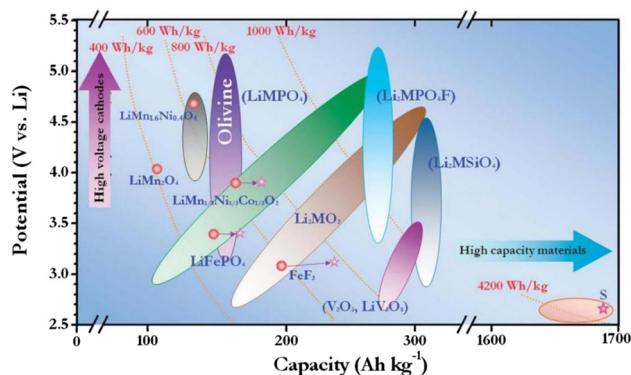† Electronic supplementary information (ESI) available. See DOI: https://doi.org/10.1039/d4tc00049h

owing to their high energy density, excellent cycling steadiness, poor self-discharge characteristics and environmental friendliness.[2,3] High energy density lithium-ion batteries have been associated with an array of issues in recent years, including deteriorating battery life and the coexistence of electrochemical side reactions that can compromise electrode integrity in harsh settings. The design of cathode materials for LIBs is fraught with numerous significant obstacles.[4,5] Therefore, enhancing the nature of lithium-ion batteries *via* the design of new and emerging materials and doping materials has emerged as a research hotspot. As can be seen from Fig. 1,[6] there is a great potential for polyanionic cathode materials: PO_4^{3-} series electrodes with high reaction potential are more suitable for large-scale energy storage systems. However, the mass and charge transport retardation of $LiMnPO_4$ severely hinders its application.[7–9] For many years, researchers have been trying to promote the property of the material. While combining conductive elements and decreasing the material's size can improve the $LiMnPO_4$ material's electrochemical performance, it has minimal effect on the material's electron–ion transport capabilities since its crystal properties remain largely unaffected.[10–13] Elemental doping can fundamentally elevate the performance of $LiMnPO_4$ materials, and one of the most widely used methods is the doping of equivalent or covalent

This journal is © The Royal Society of Chemistry 2024

J. Mater. Chem. C, 2024, **12**, 4961–4976 | **4961**

Fig. 1 Schematic diagram of the cathode material potentials of the Li-ion battery *versus* capacity, where M = Fe, Mn, Co, Ni, *etc.*

cations at Li or transition metal Mn sites.[14,15] Theoretical calculations suggest that Li site doping can reduce the electrochemical performance of $LiMnPO_4$ by blocking the conduction pathway, which in turn can cause damage to the electrochemical performance of $LiMnPO_4$. Therefore, the doping of the Li site is a matter of controversy.[16]

The electrochemical properties of lithium manganese phosphate can be effectively improved by doping manganese with various metal elements. These methods can cause dispersed metal ions $LiMnPO_4$ to provide conducting bridges, which can substantially enhance the electronic conductivity of $LiMnPO_4$ as well as the charge and discharge properties of materials. Among these, the inclusion of iron can not only solidify the material's structure and increase its energy density but it also provides the material two platforms for charging and discharging, which enhances the material's response kinetics.[17,18] For this reason, in recent years, research has been more concentrated on $Li(Mn_{1-x}Fe_x)PO_4$ composite materials. Han *et al.* prepared spherical or annular secondary particles of $Li(Mn_{1-x}Fe_x)PO_4/C$ (x = 0.2, 0.5, 0.8) using a modified polyol reaction to enhance the electrochemical performance of the $LiMnPO_4$ material.[19] $LiMn_{0.8}Fe_{0.2}PO_4/C$ is the one that shows the highest performance. It delivers a high discharge capability of 161 mA h g^{-1} at 0.05C and a capacity retention rate of 80.4% for 900 cycles at a discharge rate of 0.5C. In addition, 90% and 83% of its original capacity can be maintained at 45 °C and 55 °C after 100 cycles, respectively. Wang *et al.* selectively grew iron-doped Mn_3O_4 nanoparticles onto GO for the first time through controlled hydrolysis and solvothermal reaction with Li^+ and PO_4^{4-} to generate $Li(Mn_{1-x}Fe_x)PO_4$ single crystal nanomaterials, displaying a high specific capacity and unprecedented high power.[20] At high discharge rates of 20C and 50C, the stable capacity of the material was respectively 132 mA h g^{-1} and 107 mA h g^{-1}, and 85% and 70% at 0.5C (155 mA g^{-1}). Li^+ can diffuse rapid in the y-direction of [100], setting the stage for complex hybrid materials design and engineering and advanced energy storage with graphene.

Because iron and manganese are transition metals and occupy the same lattice in the material, the properties are more similar and can be highly compatible; thus, $Li(Mn_{1-x}Fe_x)PO_4/C$

(x = 0, 1/24, 1/12, 1/8, 1/4) materials can be formed.[21–24] In this paper, based on carbon coating, the doping modification of the transition metal potential of the positive polyanionic $LiMnPO_4$ material is investigated experimentally. $Li(Mn_{1-x}Fe_x)PO_4/C$ (x = 0, 1/24, 1/12, 1/8, 1/4) electrode was successfully prepared the by hydrothermal method, and its performance was tested. The electrochemical performances of the materials with different doping amounts were compared, and the best Fe content was selected. Simultaneously, in order to better understand and support experimental phenomenon, first principles were applied to explain the reasons for the differences in electrochemical properties from the electronic structure.

2 Experiment and calculation

2.1 The synthesis of the $Li(Mn_{1-x}Fe_x)PO_4/C$ cathode

All of the drug solutions employed in this research were of analytical reagents, and all of them were planned using deionized water. The technological process is shown in Fig. 2, and the detailed operation steps can be summarized as follows.

First, $LiOH \cdot H_2O$ crystal of a certain mass was weighed according to the ratio of the quantities of matter in the composite $Li(Mn_{1-x}Fe_x)PO_4/C$. A 200 mL solution of $LiOH \cdot H_2O$ was prepared and placed in a constant temperature collecting heating stirrer to heat up to a certain temperature. For the chemical reaction, 50 mL of the H_3PO_4 standard solution was mixed in the warm $LiOH \cdot H_2O$ liquor, and the rate of acceleration of the drop was controlled until the white precipitate was fully precipitated. Li_3PO_4 grey powder was obtained after standing at room temperature for 1 h, followed by washing, frying, sieving, and calcination.

Then, crystals of $MnSO_4 \cdot H_2O$ and $FeSO_4 \cdot H_2O$ of a certain mass were weighed according to the ratio of the quantities of material in the $Li(Mn_{1-x}Fe_x)PO_4/C$ composite material. Both crystals were dissolved in a 36 mL mixed solution of PEG400–H_2O with the off-white powder Li_3PO_4 synthesized, where the ratio of the volumes of PEG400–H_2O was 1 : 2. After stirring, the resulting mixture was transferred to a 50 mL PTFE-lined reactor and reactor at 160 °C for 9 hours. The powder $Li(Mn_{1-x}Fe_x)PO_4$ was obtained by cooling the solution to room temperature, washing, vacuum drying and sieving.

Lastly, the $Li(Mn_{1-x}Fe_x)PO_4$ powder was thoroughly mixed with vitamin C to a certain percentage, and the mixed slurry was stirred in a ball mill for 3 hours (adding 20 mL anhydrous ethanol). The precursor powder was obtained by drying the mixed slurry in an oven at 80 °C for 8 h. The $Li(Mn_{1-x}Fe_x)PO_4/C$ composites were prepared by sintering in a tube at 550 °C for 3 hours in nitrogen atmosphere.

2.1.1 Materials characterization. An X-ray diffractometer (SmartLab type) is used to investigate the crystalline phase of materials. The radiation source is the Cu-target Kα ray with a wavelength of λ = 1.544426 Å, an operating voltage of 40 kV and a scan rate of 0.04° s^{-1}. The morphologies of all the samples could be observed using an FEI Quanta200 field scanning electron microscope (SEM) and X-ray energy dispersive
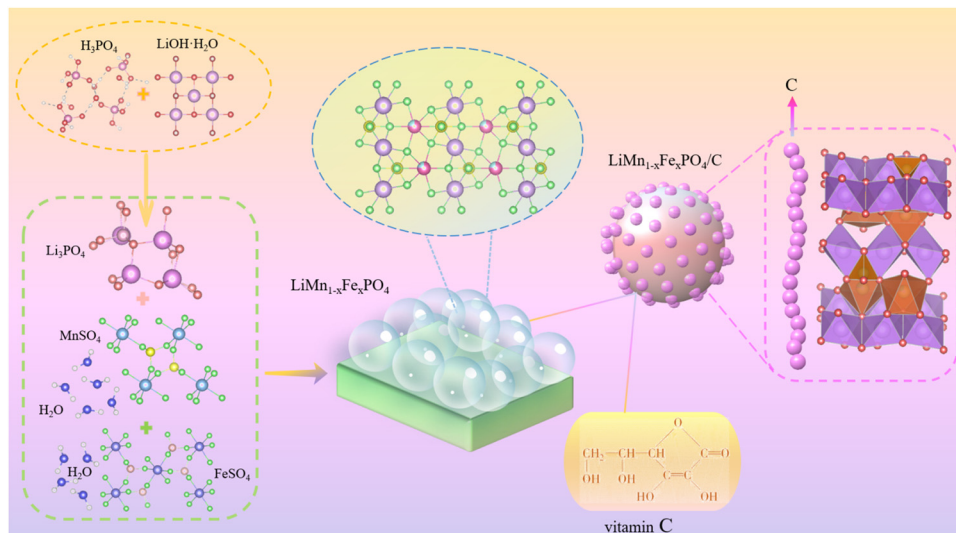
4962 | *J. Mater. Chem. C*, 2024, **12**, 4961–4976

This journal is © The Royal Society of Chemistry 2024

Fig. 2 The plot of the Li(Mn$_{1-x}$Fe$_x$)PO$_4$/C (x = 0, 1/24, 1/12, 1/8, 1/4) composite material.

spectrometer (EDS). XPS measurements were carried out using a monochromatic Al Kα excitation source ($h\nu$ = 1486.6 eV) on the ultra X-ray photoelectron spectrometer equipped with a Kratos Axis instrument.

2.1.2 Electrochemical performance test. The electrode material, acetylene black and polyvinylidene fluoride (PVDF) were mixed in N-methylpyrrolidone (NMP) at a ratio of 8:1:1. After the resulting slurry was evenly coated on the aluminium foil, in order to enhance the uniformity and density of the electrode, the slurry was extruded onto the electric roller. The slurry was allowed to dry in a vacuum oven at 120 °C for 8 h. The stack of CR2032 buttons was assembled in a glove box filled with high-purity argon using Celgard 2400 as the diaphragm with the electrode material prepared as the positive electrode and the Li metal as the opposing electrode. The electrolyte has a design and a ratio of 1.0 M LiPF$_6$ in EC:DMC:EMC = 1:1:1 vol%. A CT2001A LAND battery tester was used to measure the charge–discharge and cycling properties under constant current for the 2.5–4.5 V voltage range. Impedance and CV tests were performed at Shanghai Chenhua Electrochemistry Workstation (CHI660E).

2.2 Computing method

All crystal structure plots were drawn in the VESTA software package, and the computational process was performed using the VASP software package. The geometry, lattice vectors and atomic coordinates of the initial crystal of Li(Mn$_{1-x}$Fe$_x$)PO$_4$/C were optimized using the conjugate gradient (CG) method until the forces acting on each relaxation atom were less than 0.05 eV Å^{-1}. The energy of the optimized crystal structure was calculated, including the state density, energy band and population of the material. The SCF convergence standard for electronic self-consistent calculation was 1.0×10^{-8} eV atom^{-1}, and the calculation converges completely when the energy change of the system is below the set of convergence values.

The exchange correlation energy was handled in the pin-polarized generalize-gradient-approximation (GGA) with the Perdew–Burke–Ernzerhof (PBE) formula. Considering the correlation of electrons in Mn-3d and Fe-3d orbitals in Li(Mn$_{1-x}$Fe$_x$)PO$_4$ cells, a Hubbard-like correction (GGA+U) was added to the total energy functional for correction, the effective U values of Mn and Fe were set respectively at 3.9 eV and 5.3 eV, and the cutoff kinetic energy of the wave function in the plane wave was set at 520 eV. In order to fully converge the stress, the Monkhorst–Pack method was used to integrate the Brillouin region. A 2 × 2 × 2 k grid was used for structural relaxation, and a 4 × 4 × 4 k grid was used for energy minimization calculation.

3 Results and discussion

3.1 Phase and structural characterization

Fig. 3(a) exhibits the X-ray diffraction (XRD) patterns of Li(Mn$_{1-x}$Fe$_x$)PO$_4$/C composites with different Fe doping amounts. As can be seen from the figure, under the four addition amounts, the materials all have the same obvious diffraction peak as the pure phase, and all of them correspond to all the spectral lines in the JCPDF standard card (33-0803). Therefore, the introduction of Fe does not significantly affect the XRD pattern of the material and does not alter the main phase structure of the LiMnPO$_4$ material. Each Li(Mn$_{1-x}$Fe$_x$)PO$_4$/C electrode diffraction peak shape is sharp, indicating good crystallinity.

It can be obtained from the magnification in Fig. 3(b) that in the range 2θ = 28–36°, the diffraction peaks of materials with Fe doping amount of x = 1/24, 1/12, 1/8, and 1/4 have small shifts successively, indicating that Fe elements have successfully entered the LiMnPO$_4$ lattice, and the offset increases as the amount of Fe doping is increased. The fact that there isn't a C diffraction peak in the diagram indicates that the carbon layer that was created during the experiment has good dispersion and is an amorphous phase devoid of independent crystal formation. Therefore, the synthesized material has a single crystalline phase, namely, the olivine structure under the Pnma
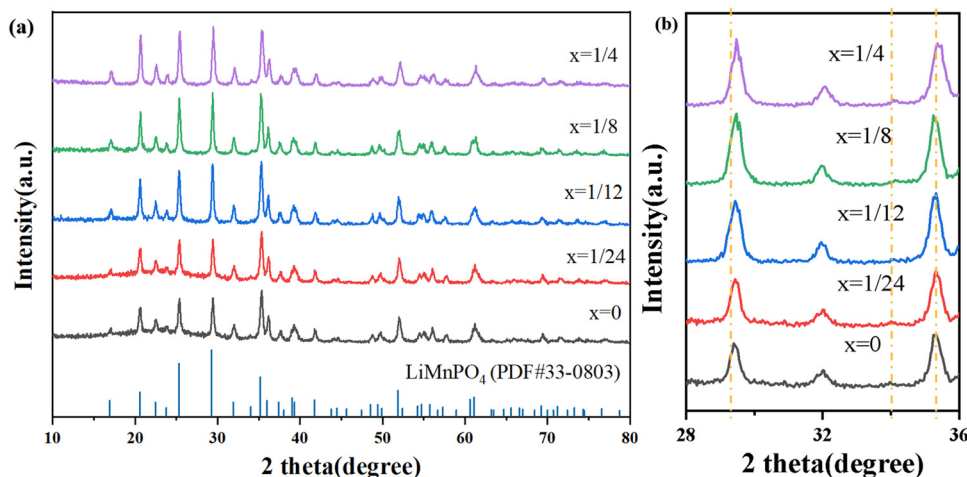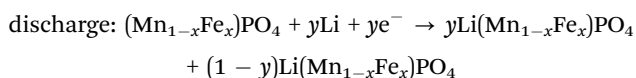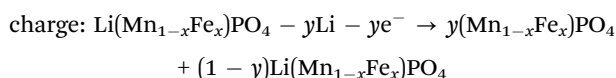
This journal is © The Royal Society of Chemistry 2024

J. Mater. Chem. C, 2024, **12**, 4961–4976 | **4963**

Fig. 3 The XRD patterns of $Li(Mn_{1-x}Fe_x)PO_4/C$ materials.

space group. In order to determine the actual composition of the $Li(Mn_{1-x}Fe_x)PO_4/C$ (x = 0, 1/24, 1/12, 1/8, 1/4) samples, ICP was used for characterization, as shown in Table 1.

The XRD patterns of the $Li(Mn_{1-x}Fe_x)PO_4/C$ samples were further refined according to the Rietveld method, as evidenced from Fig. 4. The least square method was used to fit the diffraction peak of the sample $Li(Mn_{1-x}Fe_x)PO_4/C$, and the lattice parameters of the sample were obtained (see Table S1, ESI†). It was found that they were basically unchanged within the measurement error range. The lattice parameters of the Fe-doped sample showed little change compared to pure $LiMnPO_4/C$, suggesting that $Li(Mn_{1-x}Fe_x)PO_4/C$ fundamentally maintained the crystal structure in accordance with the initial $LiMnPO_4/C$ material. As the Fe doping is increased, the value of c/a increases, indicating that the doping reduces the cation mixing and $LiMn_{3/4}Fe_{1/4}PO_4/C$ is optimal. Since Mn^{2+} has a larger ionic radius than Fe^{2+}, the size of the cell should theoretically decrease when Fe^{2+} replaces Mn^{2+}. From the data in Table S1 (ESI†), the volume of the $Li(Mn_{1-x}Fe_x)PO_4/C$ system gradually decreases with the increase in doping, which provides evidence that the crystal structure of the $Li(Mn_{1-x}Fe_x)PO_4/C$ material with Fe dopant sites has been produced.

The two phase mechanism of Li^+ insertion and removal in the main structure during the charging and discharging of the $Li(Mn_{1-x}Fe_x)PO_4$ positive electrode material can be represented by the equation below. The radius of the Fe ion is smaller than that of Mn ion; thus, the introduction of Fe reduces the lattice spacing and helps to boost the diffusion channel of lithium-ion in $LiMnPO_4$.

$$\text{charge: } Li(Mn_{1-x}Fe_x)PO_4 - yLi - ye^- \rightarrow y(Mn_{1-x}Fe_x)PO_4$$
$$+ (1-y)Li(Mn_{1-x}Fe_x)PO_4$$

$$\text{discharge: } (Mn_{1-x}Fe_x)PO_4 + yLi + ye^- \rightarrow yLi(Mn_{1-x}Fe_x)PO_4$$
$$+ (1-y)Li(Mn_{1-x}Fe_x)PO_4$$

In order to gain a detailed understanding of the effect of Fe introduction on the crystal construction of $LiMnPO_4$, the

Table 1 Main chemical composition of $Li(Mn_{1-x}Fe_x)PO_4/C$ (wt%)

x	Li	Mn	Fe	P	O	C
0	4.07	32.58	0	18.28	37.83	7.13
1/24	4.11	31.15	1.41	18.31	37.84	7.03
1/12	4.16	29.41	2.59	18.35	37.86	7.09
1/8	4.13	28.39	4.17	18.29	37.75	7.15
1/4	4.09	24.26	8.36	18.27	37.79	7.08

$Li(Mn_{1-x}Fe_x)PO_4$ doping system of $LiMnPO_4$ expanded super-cell was established using the VESTA modeling software. In order to prevent doping atom aggregation, the model was constructed using the random dispersion doping principle, with the proportions of Fe and Mn set at 1 : 23, 1 : 11, 1 : 7, and 1 : 3 (Fig. S1, ESI†). Table S2 (ESI†) shows the mean bond length of Li–O, Mn–O, P–O and Fe–O bonds of atoms near the center of the $Li(Mn_{1-x}Fe_x)PO_4$ crystal and the changes in the O–P–O bond angles that make up PO_4 tetrahedron. After Fe doping, P–O bond length and O–P–O bond angle do not change significantly, indicating that the main structure of the crystal composed of PO_4 tetrahedron changes little, and $Li(Mn_{1-x}Fe_x)PO_4$ still retains the same skeleton structure of the lattice as that of the raw material $LiMnPO_4$, with a good structural stability. In contrast, Mn–O bonding is shorter than that of Fe–O bonding; a slight change in the lattice constant after doping may be caused by this. Changes in the bond length and bond angle cause the orthogonal structure to shrink inward or outward, which can change the spread of Li^+, thereby affecting the electrochemical performance of the material in question. Therefore, doping may improve the electronic conductivity of the $LiMnPO_4$ electrode, and only doping $LiMnPO_4$ with appropriate Fe concentration can enhance the electrochemical performance of the material. Compared with the undoped Li–O bond, the bond length increases after doping, stating that the formed binding energy between lithium ion and oxygen ion decreases after doping, which favors the de-intercalation of Li^+ and, to a certain extent, the spread rate of
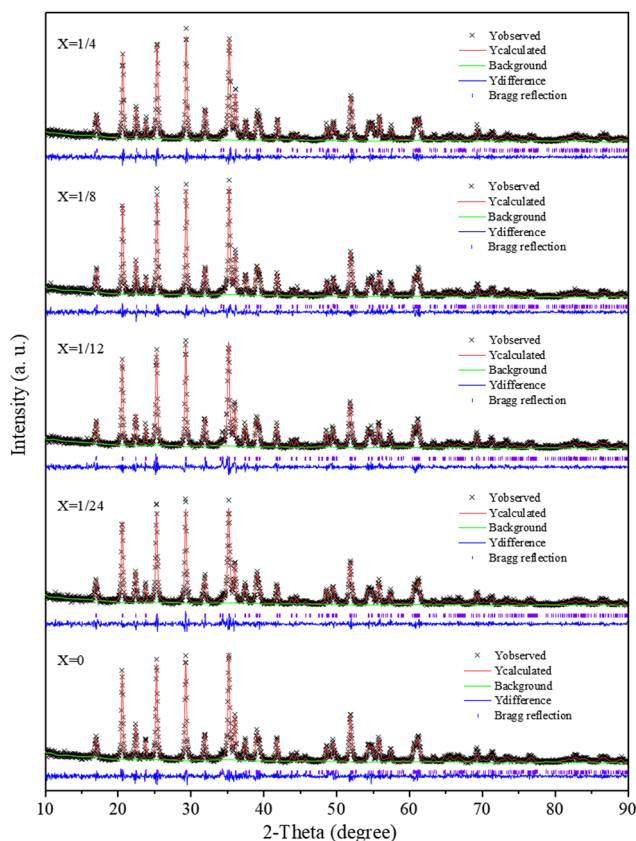
Fig. 4 The Rietveld patterns of Li(Mn$_{1-x}$Fe$_x$)PO$_4$/C materials.

Li$^+$ is increased. With an Fe doping level of 1/4, the Li–O of the biggest sample, LiMn$_{3/4}$Fe$_{1/4}$PO$_4$, is more favorable to lithium-ion de-intercalation in principle. This lowers the activation energy involved in the insertion and removal of lithium ions and effectively increases the electrical conductivity.

The process of Li$^+$ migration can be regarded as an inverse process of Li vacancy migration; when calculating Li$^+$ migration in VASP software, the formation energy of Li vacancy (denoted as E_1) should be calculated first, and then Li ion should be placed in the middle position of the Li migration process to find the maximum formation energy E_2 through transition state search, and then the diffusion barrier $\Delta E = E_1 - E_2$, which is the difference in formation energy between the two calculations. Studies have shown that when lithium ions in the olivine structure LiMnPO$_4$ (*Pnma*) are diffused along the b axis, the migration barrier in the diffusion process is the smallest,[25] and its diffusion path is a 1-dimensional channel.

To gain insight into the charge transfer in the bonding process of Li(Mn$_{1-x}$Fe$_x$)PO$_4$ materials' binding process after Fe doping, Table S3 (ESI†) shows the average net charge of atoms in the expanded Li(Mn$_{1-x}$Fe$_x$)PO$_4$ system. The initial valence electron configurations of Li, O, P, Fe and Mn atoms in the material are as follows: 2s^1, 2s^{2}2p^4, 3s^{2}3p^3, 3d^{6}4s^2, 3d^{5}4s^2; the outermost electron numbers of Li, O, P, Mn and Fe elements are respectively taken as 1, 6, 5, 7 and 8. The net charge numbers of Li, P, Mn and O in the Li(Mn$_{1-x}$Fe$_x$)PO$_4$ are close to those of the initial LiMnPO$_4$ material at each doping

amount. It is obvious that the net charge number of Fe atom is larger than that of Mn atom in Fe doped material, indicating that Fe atom transfers more electrons. The atom that forms a covalent connection with O will have a higher covalent component and a larger net charge (Mulliken atomic charges) due to the larger charge transfer. It can be observed from Table S3 (ESI†) that the average net charge of P element in LiMn$_{3/4}$Fe$_{1/4}$PO$_4$ was the highest at 2.5872 (e), indicating that it formed the most stable P–O bond in the Li(Mn$_{1-x}$Fe$_x$)PO$_4$ system.

Fig. 5(a) renders the total XPS spectra of LiMn$_{3/4}$Fe$_{1/4}$PO$_4$/C particles, confirming the presence of the elements Mn, Fe, P, O, C and Li elements in the sample, which is in agreement with the analysis of the EDS face scan energy spectrum analysis below. The characteristic peak corresponding to the C-1s map in Fig. 5(b) verifies the existence of C in the sample. Fig. 5(b) show the corresponding characteristic peaks in the P-2p and O-1s maps. P-2p peaks at about 133.3 eV and O-1s peaks near 529.3 eV and 533.25 correspond to lattice oxygen and surface oxygen, where surface oxygen is formed by oxygen vacancies 1s. The lattice O of the orbital interacts with the P element of the 2p orbital to form the PO$_4^{3-}$ ion.

Mn^{3+} is a d^4 configuration with a high spin t$_{2g}^3(\uparrow)$ e$_g^1(\uparrow)$ state and is a typical Jahn–Teller active ion, which has also been found in other transition metal chemical compounds such as LiMnO$_2$ and LiNiO$_2$.[26] The Jahn–Teller influence can bring about the bulk and cell deformation of the electrode and ultimately cause the electrode to deteriorate mechanically.[27] Moreover, Mn^{3+} will cause Li(Mn$_{1-x}$Fe$_x$)PO$_4$/C crystal particles to become relatively large; nevertheless, too much Mn^{3+} will cause O defects, which will alter the material's electrochemical properties. Hence, the existence of Mn^{3+} ions in Li(Mn$_{1-x}$Fe$_x$)PO$_4$/C materials is detrimental to the material stability in the process of charge and discharge.

To further analyse the form of Mn presence and chemical state in the Li(Mn$_{1-x}$Fe$_x$)PO$_4$/C composite electrodes, fine-spectrum XPS tests were carried out on samples with different Fe abundances in the Mn-2p region. As can be seen in Fig. 5(c)–(g), the hybrid characteristic peaks of Mn^{3+} and Mn^{2+} are well separated on Mn-2p$_{3/2}$ and Mn-2p$_{1/2}$ orbits. Using the XPSPEAK41 software, the least square method is used to perform peak splitting fitting of the Mn-2p spectral peaks on the surface. In the XPS spectrum, Mn-2p$_{3/2}$ and Mn-2p$_{1/2}$ orbitals have been used to simulate two characteristic peaks, which indicate that Mn exists in the shape of Mn^{3+} and Mn^{2+}. As can be seen in Fig. 5(h)–(k), the hybrid characteristic peaks of Fe^{2+} and Fe^{3+} are well separated on Fe-2p$_{3/2}$ and Fe-2p$_{1/2}$ orbitals. Peak splitting fitting of the Fe-2p spectral peaks on the surface is carried out using the least square approach and the XPSPEAK41 program. Fe-2p$_{3/2}$ and Fe-2p$_{1/2}$ orbitals have been employed to simulate two distinctive peaks in the XPS spectrum that take the forms of Fe^{3+} and Fe^{2+}, respectively, and which serve as indicators that Fe is present. In the Li(Mn$_{1-x}$Fe$_x$)PO$_4$/C material, the energy of the orbital is less than that of the pure phase LiMnPO$_4$/C. Subsequent investigation showed that doping altered the peak area and half-peak width of Mn^{3+} and Mn^{2+}, which is considered to have caused variations in the
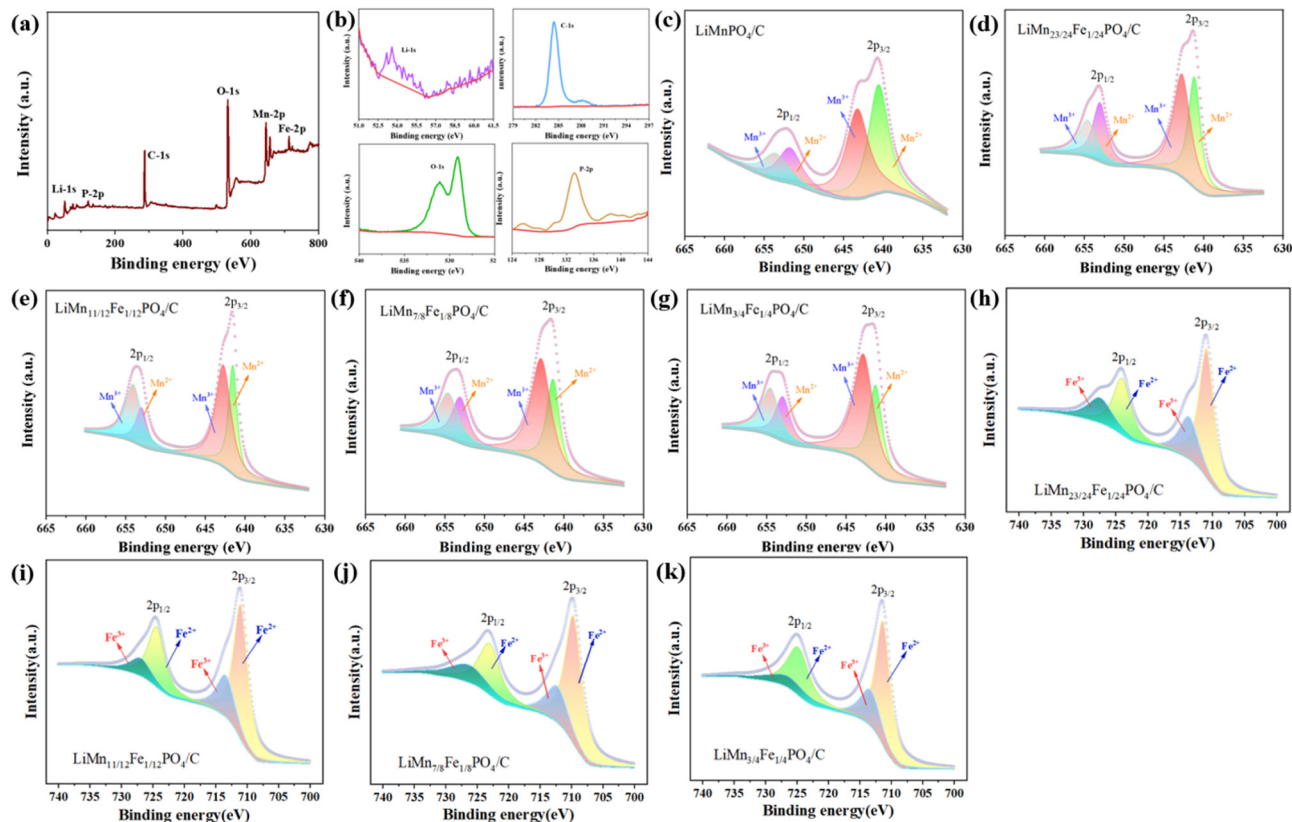
This journal is © The Royal Society of Chemistry 2024

J. Mater. Chem. C, 2024, **12**, 4961–4976 | **4965**

Fig. 5 XPS spectra of LiMn$_{3/4}$Fe$_{1/4}$PO$_4$/C composites: (a) total energy spectrum; (b) the Li element in the 1s orbital, the C element in the 1s orbital, the P element in the 2p orbital and the O element in the 1s orbital; (c)−(g) Mn 2p orbital XPS profiles of the Li(Mn$_{1−x}$Fe$_x$)PO$_4$/C sample; (h)−(k) Fe 2p orbital XPS profiles of the Li(Mn$_{1−x}$Fe$_x$)PO$_4$/C sample.

relative concentrations of Mn^{3+} and Mn^{2+} in the Li(Mn$_{1−x}$Fe$_x$)PO$_4$/C electrode. The content of Mn^{2+} was estimated by the ratio of the peak areas of Mn^{2+}/(Mn^{2+} + Mn^{3+}) in the Mn 2p$_{3/2}$ and Mn 2p$_{1/2}$. It is not difficult to see that the Mn^{2+} decreased content gradually increases with increasing amount of Fe doping. Mn^{2+} makes the relatively large Li(Mn$_{1−x}$Fe$_x$)PO$_4$/C crystal particles. Thus, the higher the iron content, the smaller the volume of the material, which is accordance with the further refinement of XRD in Fig. 4. As a result, the LiMn$_{3/4}$Fe$_{1/4}$PO$_4$/C material performs excellently.

The SEM topography and the EDS of the Li(Mn$_{1−x}$Fe$_x$)PO$_4$/C are depicted in Fig. 6. The morphology of the Li(Mn$_{1−x}$Fe$_x$)PO$_4$/C system is primarily spherical accumulation, with numerous small particles attached above, forming materials with different grain sizes. The spherical Li(Mn$_{1−x}$Fe$_x$)PO$_4$/C electrode has a large specific superficial area, which can offer more electrochemistry activated sites for the fast de-intercalation of Li$^+$, effectively diminishing the concentration polarization. There was no significant change in the grain size with the increase in Fe content. The four synthetic samples have similar grain shapes and are spheroid and small in size. The complete removal of Li$^+$ from the electrode material and the full release of material capacity are ensured by the fine dispersion of the lithium positive material, which additionally enables the material to fully permeate the electrolyte and ensures its wettability.

Careful observation states that the crystalline size of the LiMn$_{3/4}$Fe$_{1/4}$PO$_4$/C material seems to be finer, and the fine uniform electrode material makes for the rapid removal of lithium ions and the improvement of electrochemical performance. Moreover, it is observed that the material has a multistage layered structure consisting of micropores and macrospores, which can supply enough cushion area for the change of volume produced by the lithium insertion and removal process, improve the structure stability of material and thus promote its cyclic stability. As can be seen from Fig. S4 (ESI†), manganese, iron, oxygen, phosphorus, and carbon on the surface of the material are evenly distributed throughout the measured samples and are in agreement with the SEM morphology of the material. Additionally, when Fe doping increases, Mn content also gradually drops, and both elements' atomic percentages are essentially consistent with the doping ratio. Roughly speaking, the atomic percentage of each element (At%) is line with the ratio of LiMn$_{3/4}$Fe$_{1/4}$PO$_4$/C; in particular, the ratio of manganese and iron is synthesized in strict accordance with 3 : 1. It is also possible to expose LiMn$_{3/4}$Fe$_{1/4}$PO$_4$/C composite to be tightly and evenly enclosed by amorphous carbon layers of formless construction. A homogeneous carbon layer is formed by the carbonation of ascorbic acid during high temperature roasting. The carbon layer can direct more electrons into the periphery of the active material, allowing it to smoothly enter the lithium-ion entrapment process.
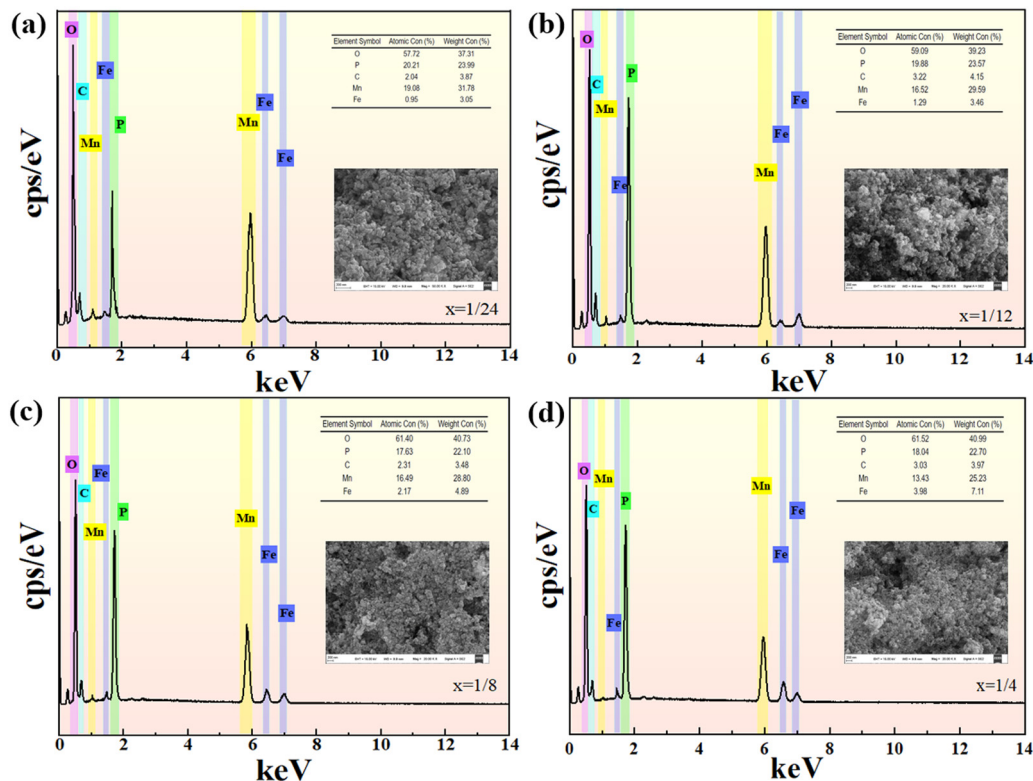
4966 | *J. Mater. Chem. C*, 2024, **12**, 4961–4976

This journal is © The Royal Society of Chemistry 2024

Fig. 6 The SEM images and EDS spectra of Li(Mn$_{1-x}$Fe$_x$)PO$_4$/C.

More importantly, the dispersed amorphous C layers at the periphery of the LiMn$_{3/4}$Fe$_{1/4}$PO$_4$ grains are interconnected to form a three-dimensional network structure, which can effectively inhibit the agglomeration of LiMn$_{3/4}$Fe$_{1/4}$PO$_4$ grains, facilitate fast electron transport, and allow the ability of the electrode material to be completely released.

The micro-crystal structure of the LiMn$_{3/4}$Fe$_{1/4}$PO$_4$/C cathode material is displayed in Fig. 7. The transmission electron microscopy (TEM) images of the grains demonstrate that they are polished on the particle surface and have high crystallinity (Fig. 7(a)). Fig. 7(b) depicts an image created using the fast Fourier transform (FFT). LiMn$_{3/4}$Fe$_{1/4}$PO$_4$/C has an approximate plane spacing (adjacent lattice fringe spacing) of 3.73 Å, which is equal to the d values of the (101) plane on the LMFP material standard card. LiMn$_{3/4}$Fe$_{1/4}$PO$_4$/C has clear and continuous lattice fringes and smooth grain edges, which correspond to the XRD results and represent the sample's good clarity. The area of the particles used in SAED analysis is depicted in Fig. 7(c). The selected region electron diffraction illustrates both the polycrystalline nature of the fabricated cathode materials and the decrease in the ring diffraction patterns of the polycrystalline samples. The *hkl* graphs of the subsequent LMFP composites, respectively, correlate to the observed notable ring patterns: (101), (200/121), (211), and (312).

3.2 Electrochemical performance

Fig. 8(a) states the initial charge–discharge curve of the Li(Mn$_{1-x}$Fe$_x$)PO$_4$/C composite material at 1C, which is charged to a voltage of 4.5 V, then discharged to 2.5 V. Below this voltage, the charging and discharging platforms close to 4.2 V
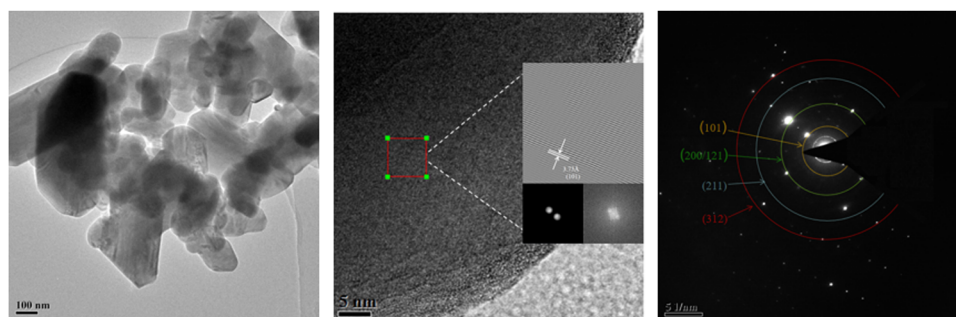

Fig. 7 (a) TEM image, (b) HRTEM image, and (c) SAED pattern of LiMn$_{3/4}$Fe$_{1/4}$PO$_4$/C cathode materials.

and 4.0 V respectively correspond to the lithium insertion and removal processes and to the oxidation and reduction potential of Mn^{2+}/Mn^{3+}, accompanied by the valence state change of the manganese ion. The platform capacity improves inch by inch with the enhancement of the iron doping content. As can be described in the figure, each material displays a better specific discharge capability. The discharge capacities of $LiMn_{3/4}Fe_{1/4}PO_4/C$, $LiMn_{7/8}Fe_{1/8}PO_4/C$, $LiMn_{11/12}Fe_{1/12}PO_4/C$, $LiMn_{23/24}Fe_{1/24}PO_4/C$ and $LiMnPO_4/C$ are respectively 141.6, 135.7, 131.1, 123.8 and 113.3 mA h g^{-1}, and these values are higher than that of the pure phase material, indicating that introducing a proper amount of Fe can indeed enhance the electrochemical performance of the material. This is because the redox reaction has good reversibility, which means that it has good dynamic characteristics and greatly enhances the specific discharge capacity at a high voltage. It also has minimal polarization phenomenon when the material acts as the electrode. Finally, the underlying discrepancy between the charge and discharge plateaus of the electrodes at this doping amount is minimal. Furthermore, the presence of Fe also enhances the spread of Li^+, thereby significantly enhancing the conductivity of the material. It is worth mentioning that the $LiMn_{3/4}Fe_{1/4}PO_4/C$ sample has a more stationary and longer discharge voltage plateau with the best discharging capacity, indicating the excellent rate performance potential.

500 cycle tests were performed on $Li(Mn_{1-x}Fe_x)PO_4/C$ electrode materials with different amounts of Fe doping at 1C, as evidenced from Fig. 8(b). During the cycle, the specific discharge ability of each electrode was mildly reduced. As the addition of Fe increases, the specific discharge ability of the material progressively increases. The presence of Fe has improved the intrinsic electroconductibility of $Li(Mn_{1-x}Fe_x)PO_4/C$ materials; thus, the recycling properties of materials have also been improved. After 500 cycles of charge and discharge, the discharge capacities of $LiMnPO_4/C$, $LiMn_{23/24}Fe_{1/24}PO_4/C$, $LiMn_{11/12}Fe_{1/12}PO_4/C$, $LiMn_{7/8}Fe_{1/8}PO_4/C$ and $LiMn_{3/4}Fe_{1/4}PO_4/C$ were 107.0, 118.4, 127.0, 132.2 and 138.6 mA h g^{-1}, and the capacity retention rates were 94.44%, 95.64%, 96.87%, 97.42% and 97.88%, respectively. Clearly, $LiMn_{3/4}Fe_{1/4}PO_4/C$ has superb cyclic properties and a high invertible capacity, and the attenuation of capacity is minimal. In addition, it can be seen from Fig. 8(c) that after 500 battery cycles, the particles of $x = 1/4$ of the material are relatively complete and uniform, indicating that the $LiMn_{3/4}Fe_{1/4}PO_4/C$ material structure is more stable.

The rate performance of the electrode is critical for LIBs. The rate performance curve for the $Li(Mn_{1-x}Fe_x)PO_4/C$ cathode materials is described in Fig. 8(d). Each sample is within the 2.5–4.5 V voltage range. The power was then sequentially loaded at 1C, 1.5C, 2C, and 3C ratios for 25 weeks, and then
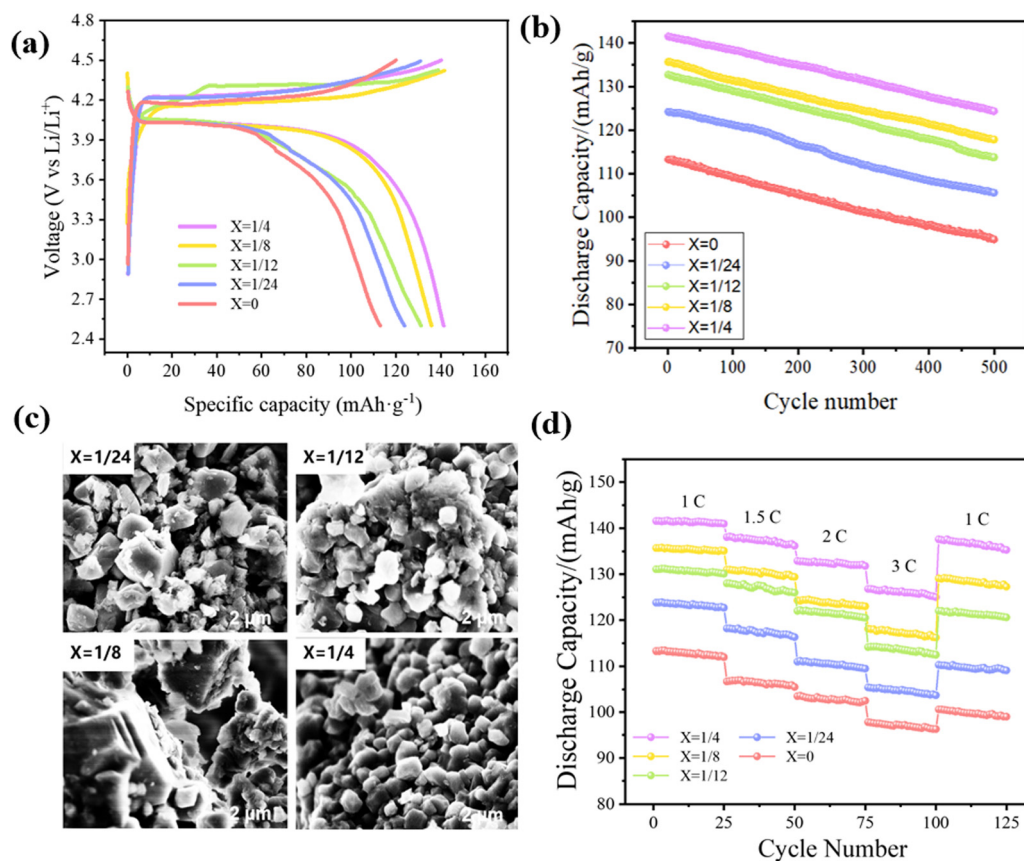

Fig. 8 (a) The initial charge and discharge curves of $Li(Mn_{1-x}Fe_x)PO_4/C$ at 1C. (b) The cycling performance of the $Li(Mn_{1-x}Fe_x)PO_4/C$ sample at 1C. (c) SEM images of $Li(Mn_{1-x}Fe_x)PO_4/C$ after 500 cycles. (d) The rate capability of the $Li(Mn_{1-x}Fe_x)PO_4/C$ sample.

4968 | *J. Mater. Chem. C*, 2024, **12**, 4961–4976

This journal is © The Royal Society of Chemistry 2024

it went back to the original 1C ratio. As illustrated in the diagram, with the gradual improvement in the discharging rate, the discharging capacity of the Li(Mn$_{1-x}$Fe$_x$)PO$_4$/C electrode is a step-like attenuation, which is a common phenomenon of LIB. After 125 weeks of rate testing, the recovery capacities of LiMn$_{3/4}$Fe$_{1/4}$PO$_4$/C, LiMn$_{7/8}$Fe$_{1/8}$PO$_4$/C, LiMn$_{11/12}$Fe$_{1/12}$PO$_4$/C, LiMn$_{23/24}$Fe$_{1/24}$PO$_4$/C and LiMnPO$_4$/C is respectively 135.3, 127.3, 120.6, 109.1, and 99.0 mA h g^{-1} at 1C. As a consequence, the LiMn$_{3/4}$Fe$_{1/4}$PO$_4$/C electrode performs noticeably better than other materials under the same circumstances, with better structural integrity and reversibility, and it displays a reasonably excellent discharge capacity at any discharge current density. This is due to the fact that the proper doping of Fe enhances the electron/ionic electroconductibility of the material, promotes redox activity, and then alleviates the structural slumping created by the instability of the removal phase of Mn$_{3/4}$Fe$_{1/4}$PO$_4$/C in the charging–discharging process of the LiMn$_{3/4}$Fe$_{1/4}$PO$_4$/C nano-electrode. It is worth mentioning that the doping amount of Fe is higher than that of pure LiMnPO$_4$/C material even at 1/24, thus confirming that the entrance of Fe can indeed enhance the discharge capability of the material.

In order to understand the reason why transition metal Fe doping improves electrochemistry, we start from the electronic construction of the Li(Mn$_{1-x}$Fe$_x$)PO$_4$ system, taking the comparison of the amount of occupied states near Fermi as the starting point and making the analysis of the total state density

(TDOS) of spin polarized supercell systems and the wave state density (PDOS) of Li-s, Li-p, Fe-4s, Fe-3p, Fe-3d, Mn-4s, Mn-3p, Mn-3d, P-2s, P-2p, O-2s and O-2p in Li(Mn$_{1-x}$Fe$_x$)PO$_4$ materials.

Fig. 9(a) exhibits the total state density of the Li(Mn$_{1-x}$Fe$_x$)PO$_4$ system at each doping amount. From the figure, it can be observed that the total state density shifts to the low energy in the presence of iron doping, resulting in the conduction band passing through the Fermi appearance at the bottom, which in turn results in an increase in the number of conduction bands. Since the number of valence electrons is equal to the integral of the horizontal and vertical axes with respect to the density of states, the larger the supercell, the greater the total number of valence electrons, and hence the larger the ordinate. In this paper, the supercell with each doping amount contains 192 atoms, which is a large model; thus, the vertical coordinates are −250–250 states per eV. The Li(Mn$_{1-x}$Fe$_x$)PO$_4$ system of total state density data including energy, spin up states and spin down states, by looking for energy values near the Fermi level (0), an energy difference between a maximum occupied state (HOMO) and a minimum unoccupied state (LUMO) can be used to determine a material band gap at each doping amount. Li(Mn$_{1-x}$Fe$_x$)PO$_4$ material bandgaps of x = 1/24, 1/12, 1/8 and 1/4 are 3.586 eV, 3.525 eV, 3.515 eV and 3.503 eV, respectively. The band gap is related to the difficulty of electron transition in the material: the smaller the band gap, the less energy is needed for electron transition,
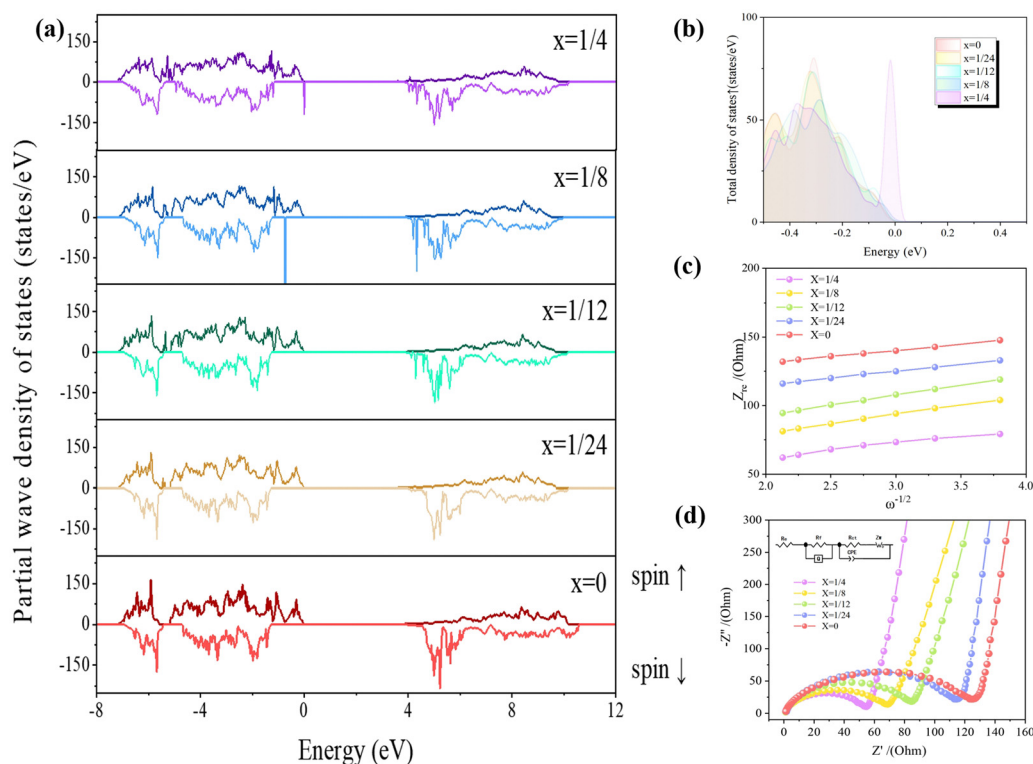

Fig. 9 (a) Total density of states map of the Li(Mn$_{1-x}$Fe$_x$)PO$_4$ system (drawing from the comparison of the amount of occupied states near the Fermi level). (b) Comparison of total density of states (TDOS) of Li(Mn$_{1-x}$Fe$_x$)PO$_4$ systems near the Fermi level. (c) Nyquist impedance spectroscopy of Li(Mn$_{1-x}$Fe$_x$)PO$_4$/C cathode materials (illustration shows the corresponding equivalent circuit). (d) Linear matching of low frequency between Z$_{re}$ and ω$^{-1/2}$ to Li(Mn$_{1-x}$Fe$_x$)PO$_4$/C.

This journal is © The Royal Society of Chemistry 2024

J. Mater. Chem. C, 2024, **12**, 4961–4976 | **4969**

and more easily the electron transition will be; thus, the conductivity can be summarized as $x = 0 < x = 1/24 < x = 1/12 < x = 1/8 < x = 1/4$. This may be due to the fact that the conductivity of Fe should be better than that of Mn; thus, the more Fe in the system, the more the occupied states near the Fermi level.

In order to illustrate the optimal doping amount of the $Li(Mn_{1-x}Fe_x)PO_4$ system, Fig. 9(a) has been detailed to give a comparison of the total state density in the spin up near the Fermi level $[-0.5 \text{ eV}, 0.0 \text{ eV}]$, as shown in Fig. 9(b). According to the thickness of states near the Fermi level, the best doping quantity can be judged theoretically. The closer the electrons are to the Fermi level, the easier they transition, the more occupied states they have, and the better their conductivity. From Fig. 9(b), it can be seen intuitively that $[0.0 \text{ eV}]$ corresponds to Fermi level, moving from $[0.0 \text{ eV}]$ to the negative direction; the material that is encountered first will indicate the material that has more occupied states. It can be found that the total state density of the $LiMn_{3/4}Fe_{1/4}PO_4$ crystal is closest to the Fermi level $[0.0 \text{ eV}]$, indicating that more electrons in the valence band of the material can be used to transition to the conduction band at this doping amount; thus, its electrical conductivity is the best.

Fig. S4 (ESI†) shows the split-wave state density of atoms in the s, p and d orbitals in $LiMnPO_4$, it can be seen that the total state density is mainly contributed by the Mn-3d state sum, O-2p state, P-2p state, Li-p state and Li-s state, while the Mn-3p state, Mn-4s state, P-2s state and O-2s state hardly contribute to the total state density. The valence states are the recombination of the d orbitals of manganese and p orbitals of oxygen. The low guidance state is mainly the Mn-d state, while the high guidance state is mainly the P-p and O-p states. Most of the spins in the Mn-d state are fully filled but only a small number of spins in the Mn-d state exist at the leading edge. The resonance between the Mn-3d and P-2p orbitals forms stable covalent bonds of Mn–O and P–O. The s orbitals of the O and P atoms are located in the low energy region. In addition, the valence states near Fermi level $[-0.50 \text{ eV}, 0.00 \text{ eV}]$ are mainly Mn-3d states (corresponding to low-energy bonding orbital t_2 state) and O-2p states, while the conduction bands $[2.35 \text{ eV}, 5.49 \text{ eV}]$ are mainly Mn-3d states (corresponding to high-energy bonding orbital e state) and Li-p states. The oxidation state of manganese atom in $LiMnPO_4$ is trivalent, and the high-spin channel has 4 electrons with an electron configuration of $(t_{2g})^3(e_g)^1$. When the LIB is in the process of charging or discharging, the oxidation state of manganese ion alternates between Mn^{3+} and Mn^{4+}. The energy spectrum of Mn-3d is between 8 eV, smaller than the Fermi level, and about 12 eV, larger than the Fermi level. In the final analysis, the position of the transition metal Mn-3d state primarily determines the electrical conductivity of the $LiMnPO_4$ crystal. As a result, this is a significant source for thinking about the idea of using Fe transition metal element in the site doping of the $LiMnPO_4$ crystal in order to enhance the electrical conductivity of the $LiMnPO_4$ material. To get a better understanding of the contribution of Fe doping to the electronic construction of the crystal, we respectively calculated the density of atomic states in the material with Fe doping amount of 1/24, 1/12, 1/8 and 1/4, as shown in Fig. S5–S8 (ESI†), respectively. In the $Li(Mn_{1-x}Fe_x)PO_4$ doping system, we can see that the crystal electron structures are mainly the Fe-3d, Mn-3d, O-2p, P-2p, and P-2s orbitals, showing strong localization. Li-s states and Li-p states have the weakest contribution to the valence band. After Fe replaces some Mn in $LiMnPO_4$, the Fe-3d state appears at the maximum valence band and pushes the unoccupied Mn-3d spin down band to move to the low energy region. Part of the state density of the Fe-3d orbital is still occupied by electrons at the Fermi level; thus, Fe mainly exists in the form of Fe^{2+} in the $Li(Mn_{1-x}Fe_x)PO_4$ system. The presence of the doped element Fe induces additional d states in the band gap of pure phase $LiMnPO_4$; the Fe-d orbital of $Li(Mn_{1-x}Fe_x)PO_4$ produces a few spins at the edge of the conduction band, which is responsible for the reduction of the $LiMnPO_4$ band gap. When Fe is doped, a brand-new electronic valence state appears between the energy bands, which decreases the band gap and induces a new electron state in Fe-3d.

In the $Li(Mn_{1-x}Fe_x)PO_4$ system, the initial valence electron configurations of lithium, oxygen, phosphorus, iron and manganese atoms are $2s^1$, $2s^22p^4$, $3s^23p^3$, $3d^64s^2$ and $3d^54s^2$, respectively. As can be seen from Fig. S5–S8 (ESI†), the energy band occupied by Mn-3d electrons in the samples with different doping amounts is divided into two parts, one is from -6.0 eV to the Fermi level, and the other is from 4 eV to 8.0 eV. The band occupied by Fe-3d electrons is divided into two parts, one near -5 eV and the other between 4 eV and 6.0 eV. The bands occupied by the O-2p electrons are concentrated between -7.0 eV and the Fermi level; the energy bands of P-2p and P-2s are mainly between -7.0 eV and -5.0 eV. In the $Li(Mn_{1-x}Fe_x)PO_4$ doped system, the valence states of Li, O, P, Mn and Fe are respectively +1, -2, +5, +3 and +2. The outermost electron configurations of Fe and Mn are respectively $3d^64s^2$ and $3d^54s^2$, and their d electron numbers are respectively 6 and 5. All five d electrons of Mn are filled in the spin up part, while Fe has five d electrons in the spin up part and one d electron in the spin down part, and both Mn^{3+} and Fe^{2+} exist in high spin states.

In the $Li(Mn_{1-x}Fe_x)PO_4$ doped system, spin-up and spin-down electronic states appear in both the valence band and conduction band. With the increase in the doping amount, due to the increasing contribution of the Fe-3d orbital, the spin-down electron state density peak of the Fe-3d orbital valence band near the Fermi level $[-0.50 \text{ eV}, 0.00 \text{ eV}]$ increases. The peak value of the electron state density of the Fe-3d orbital conduction band $[4.38 \text{ eV}, 6.24 \text{ eV}]$ is also increasing, and the change is increasingly obvious. The Mn-3d state density peak in the $Li(Mn_{1-x}Fe_x)PO_4$ doping system shows a little downward trend as doping increases, but there is essentially no change in the state density of other electrons or the comparable electron state density prior to doping.

To sum up, in $LiMnPO_4$ materials, all O-2p electrons participate in the valence band formation near the Fermi level in different degrees, the conduction electrons near the Fermi level

4970 | *J. Mater. Chem. C*, 2024, **12**, 4961–4976

This journal is © The Royal Society of Chemistry 2024

are composed of Mn-3d and O-2p hybrid electrons, and Mn-3d plays a major role. In $LiMn_{1-x}Fe_xPO_4$, the conduction electrons near the Fermi level are composed of Fe-3d, Mn-3d and O-2p hybrids, Fe-3d and Mn-3d play a major role, but only O-2p electrons near Fe-3d atoms are hybridized, which further explained that the energy gap of $Li(Mn_{1-x}Fe_x)PO_4$ materials is determined by Fe-3d and Mn-3d; there is O-2p electron and Fe-3d, Mn-3d electron hybridization phenomenon. In doped materials, electrons near the Fermi level are primarily made up of Fe-3d electrons.

Electrochemical impedance spectroscopy (EIS) can dynamically monitor the reaction of Li^+ and the diffusion of Li^+; it is one of the most important measuring tools for the analysis of the reaction dynamics of embedded Li^+. Fig. 9(c) reveals the Nyquist diagram of $Li(Mn_{1-x}Fe_x)PO_4/C$ positive material after 25 circulations of charge and discharge at 1C. Every sample consists of diagonal lines in the low-frequency domain and a concave semicircle in the high-frequency domain. Electrochemical polarization occurs in the high-frequency space, which is controlled by the reaction dynamic of the electrode, corresponding to the transfer of charge. The low-frequency region is dominated by the spread course of reagents or products in the electrode reactivity, and the concentration polarity phenomenon appears.[28]

In the Zsimpwin program, the following equivalent circuit is used to fit the original data.

$$R_e + (R_f \| Q) + [(R_{ct} + Zw \| CPE)] \qquad (1)$$

In the equation, R_e – Ohmic resistance related to Li^+ and electron transport *via* electrolytes, porous membranes, wires, active materials, *etc.*, and determines the charge–discharge rate performance of the electrode;[29,30] R_f – Interfacial resistance generated by diffusion migration of Li^+ through the SEI film; R_{ct} – Li^+ charge transfer resistance between the vibrant electrode material and the solution;[31] Z_W – the Warburg impedance of Li^+ in the $Li(Mn_{1-x}Fe_x)PO_4/C$ composite electrode material during the internal diffusion process is related to the sample transport mechanics of the sample, corresponding with the decrease in the low frequency area of the Nyquist plot;[32,33] CPE – double layer capacitance at the electrode interface; Q – SEI film at the electrode interface.

The $Li(Mn_{1-x}Fe_x)PO_4/C$ positive material consists of numerous interfaces and boundary of the phase. Strictly speaking, the centre of the high frequency half-circle in the Nyquist diagram is located beneath the Z' axis, *i.e.*, it becomes an arc of the circle, and there is a phenomenon of a decrease in the semicircle. The reason of half-circle rotation is concerned with the inhomogeneity of the electrode/electrolyte interface, which is most likely because the roughness of the electrode surface causes a change in the capacitance of the double layer, which leads to the fact that the charge shift resistor at points in the plane is no longer a number.[34] The Ohm impedance R_e of $LiMn_{3/4}Fe_{1/4}PO_4/C$ has the smallest intercept in the Z' direction at high frequency. Furthermore, the semicircular diameter of this material is also the smallest in the high-frequency zone, which means that the $LiMn_{3/4}Fe_{1/4}PO_4/C$ material is hopeful for

breaking through the dynamic limit and has the best charge transfer capacity so as to obtain bigger discharging level and better rate ability.[35]

All corresponding data obtained through equivalent circuit matching method are given in Table S4 (ESI†). The R_e values of each positive electrode are all low, manifesting that the electrolyte (1.0 M $LiPF_6$ in $EMC:DMC:EC = 1:1:1$ vol%) can well realize the transfer of Li^+ between the positive and negative active materials. As can be seen, for all $Li(Mn_{1-x}Fe_x)PO_4/C$ positive terminals, the R_{ct} are much larger; thus, the R_{ct} is a significant index to evaluate the charge shift resistance. In addition, a smaller R_{ct} can speed up the electron transfer and the insertion/removal within the interface between the active material and the electrolyte. It is obvious that the order of R_{ct} values of diversiform materials is $LiMnPO_4/C < LiMn_{23/24}Fe_{1/24}PO_4/C < LiMn_{11/12}Fe_{1/12}PO_4/C < LiMn_{7/8}Fe_{1/8}PO_4/C < LiMn_{3/4}Fe_{1/4}PO_4/C$, consistent with the order of cycle and rate performance.

All composite samples have linear slopes greater than $45°$ in the low frequency space, which suggests that they have a certain capacity, which is also a feature of fast Li^+ in-electrode diffusion. It can be seen from Fig. 9(c) that the Warburg component gradient of the SEI spectrum of $LiMn_{3/4}Fe_{1/4}PO_4/C$ is large at low frequencies, and it is noted in Table S4 (ESI†) that the electrode interface of the $LiMn_{3/4}Fe_{1/4}PO_4/C$ electrode has the highest double layer capacitance, which indicates that its electrochemical capacitance is higher, resulting in the highest Li^+ conduction capacity in its interior.[36] The analysis results are in agreement with the charge/discharge curve in Fig. 8(a), which proves to be a significant factor for improving the discharge ability.

The spread coefficient of Li^+ (D_{Li^+}) may be computed in terms of the following eqn (2),[37] and the calculation results are shown in Table S5 (ESI†). The results exhibit that the $LiMn_{3/4}Fe_{1/4}PO_4/C$ cathode electrode has the largest D_{Li^+}, an order of magnitude larger than other electrodes. Therefore, the $LiMn_{3/4}Fe_{1/4}PO_4/C$ material is more conducive to the removal and embedding of Li^+.

$$D_{Li^+} = \frac{R^2 T^2}{2A^2 n^4 F^4 C_{Li}^2 \sigma^2} \qquad (2)$$

In the above equation, R – ideal gas constant, whose value is 8.314 J $(mol\ K)^{-1}$; T – Kelvin temperature, which is equal to 298 Kelvin; A – surface area of the electrode surface active material, $A = 0.64\ cm^2$ in the current test; n – the quantity of electrons transferred in oxidation or reduction reactions, $n = 1$ in this experiment; F – Faraday's constant, which is 96 485 C mol^{-1}; C_{Li} – concentration of lithium ion in the material of the electrode, $C_{Li} = 0.0227$ mol cm^{-3} in the current test; σ – Warburg's impedance factor, determined by eqn (3), is in accordance with the gradient of Z_{re} in Fig. 9(d).

$$Z_{re} = R_e + R_f + R_{ct} + \sigma\omega^{-0.5} \qquad (3)$$

In the above equation, ω – angular frequency, and $\omega = 2\pi f$, where f is low frequency; R_e – Ohm resistance associated with

Li$^+$ and electron transport; R_f – interfacial resistance generated by the diffusion migration of Li$^+$ through the SEI film; R_{ct} – Li$^+$ charge shift resistance between the vibrant electrode material and the electrolyte.

In addition, the exchange current density I^0 in eqn (4) is also an important parameter for describing the dynamics features, and it can be employed to depict the electrochemical activity of the electrode material,[38] as shown in Table S5 (ESI†). The results showed that the exchange current density of LiMnPO$_4$/C was enhanced by Fe doping, and the cathode electrode of LiMn$_{3/4}$Fe$_{1/4}$PO$_4$/C was found to have the highest I^0. This is due to the fact that Fe has a higher conductivity than Mn; the more Fe in the system, the more occupied states are near the Fermi level, wherein the grain limit resistance and the charge shift resistance can be reduced effectively, the lithium ions can be transported quickly, and the exchange current density can be increased, which positively impacts the specific capacitance of the sample. To sum up, Fe = 1/4 is the ideal doping amount for preparing lithium ion battery Li(Mn$_{1-x}$Fe$_x$)PO$_4$/C cathode.

$$I^0 = \frac{RT}{nR_{ct}F} \tag{4}$$

In the above equation, R – the ideal gas constant, whose value is 8.314 J (mol K)$^{-1}$; T – Kelvin temperature, which is equal to 298 Kelvin; n – the quantity of electrons shifted in oxidation/reduction reactions, $n = 1$ in this experiment; R_{ct} – Li$^+$ charge shift resistance between the active electrode material and the electrolyte; F – Faraday's constant, which is 96 485 C mol^{-1}.

Fe introduction will increase the number of energy levels in the conduction band of the LiMnPO$_4$ material. It is discovered that the width of the band gap may be effectively reduced based on the differentiation between the conductor and the insulator as well as the energy band conclusion; the more closely the material is aligned with the conductor, the narrower the band gap and the better the conductivity. The band structure shown in Fig. S9 (ESI†) explains why the Fe-doped Li(Mn$_{1-x}$Fe$_x$)PO$_4$ system has excellent electrical conductivity. In x = 1/24, 1/12, 1/8 and 1/4 doping gradients, the introduction of Fe decreases the conduction band of LiMnPO$_4$ and the valence band shifts to the Fermi level, resulting in the phenomenon that the band gap of LiMnPO$_4$ decreases gradually. Therefore, the addition of a few Fe atoms to replace Mn atoms in the intrinsic system of LiMnPO$_4$ can increase the electrical conductivity. The band gaps of Li(Mn$_{1-x}$Fe$_x$)PO$_4$ of x = 1/24, 1/12, 1/8 and 1/4 are respectively 3.585 eV, 3.523 eV, 3.519 eV and 3.505 eV, which are basically consistent with the results of the total state density map of the system, as shown in Fig. 9(a). When Fe is 1/4, the gap width is the smallest; thus, 1/4 is the optimum concentration. In addition, when x = 1/4, the energy band fluctuation
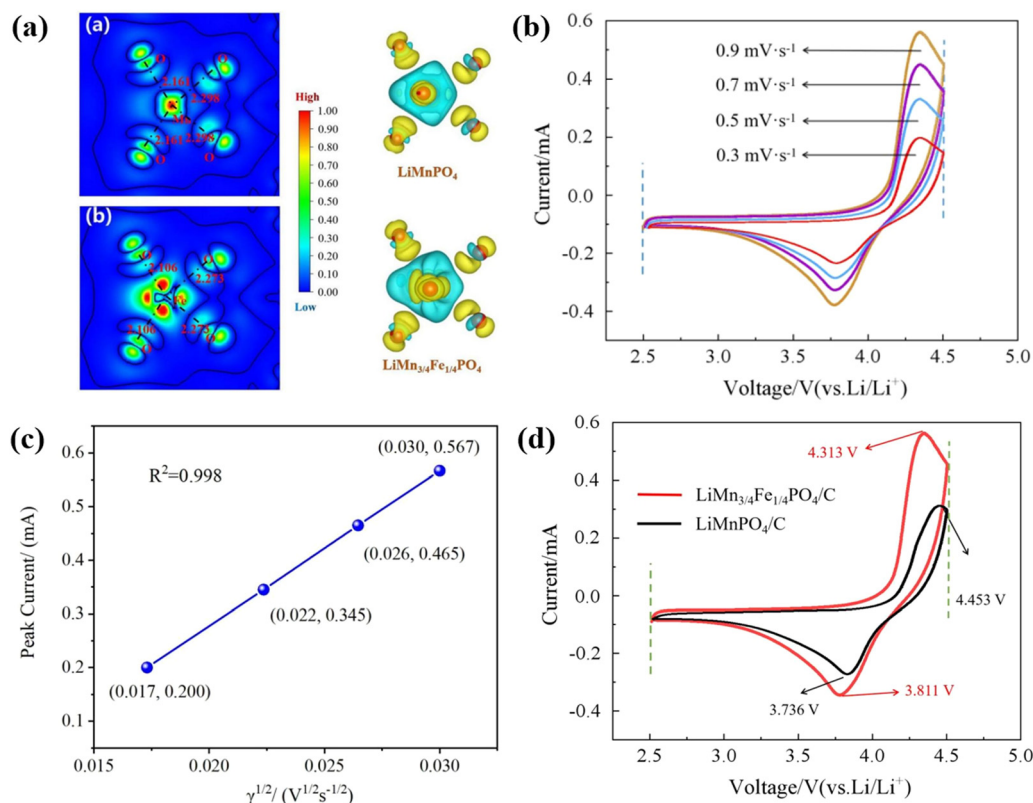

Fig. 10 Iso-surface 3D contours of the charge density difference in the de-lithiation process and planar graphs centered on Fe or Mn atom (a) between LiMnPO$_4$ and MnPO$_4$ and (b) between LiMn$_{3/4}$Fe$_{1/4}$PO$_4$ and Mn$_{3/4}$Fe$_{1/4}$PO$_4$. (b) CV profiles of the LiMn$_{3/4}$Fe$_{1/4}$PO$_4$/C material at a scanning speed of 0.3, 0.5, 0.7, and 0.9 mV s^{-1}. (c) Linear fitting of the square root of the peak redox current and scanning rate of the LiMn$_{3/4}$Fe$_{1/4}$PO$_4$/C cathode. (d) CV profiles of the LiMn$_{3/4}$Fe$_{1/4}$PO$_4$/C and LiMnPO$_4$/C electrode at a sweep speed of 0.9 mV s^{-1}.

4972 | *J. Mater. Chem. C*, 2024, **12**, 4961–4976

This journal is © The Royal Society of Chemistry 2024

around the Fermi step of the doped material is obvious, and the number of energy bands around the Fermi step is large, showing that the effective mass of electrons in these energy bands is small, and the degree of non-localization is large, the atomic orbitals composed of this energy band have a good ability to accommodate electrons, which contributes to the transport of charge carriers; thus, the $LiMn_{3/4}Fe_{1/4}PO_4$ crystal has good electrical conductivity.

The charge density difference is the difference between the superposition of the electron density of a crystal and the electron density of a neutral atom, it is beneficial to visualize the bonding properties. In Fe-doped systems, electrons are redistributed around the doped atoms. As depicted in Fig. 10(a), this paper compares the change in the electron density in space between Li_2FePO_4 and $Li_2Fe_{23/24}Mn_{1/24}PO_4$ materials after de-lithiation.

In the three-dimensional diagram to the right of Fig. 10(a), the light blue part shows the electron-loss region (charge consumption) and the yellow part shows the electron-enriched region (charge accumulation). The results show that O is a negative ion, while Mn and Fe are positive ions. Furthermore, there are clear d-orbital characteristics near Mn and Fe ions (the electron distribution is shaped like a cross), and clear p-orbital characteristics near O ions (the electron distribution is shaped like a dumbbell). This indicates that the O 2p state can efficaciously coincide with the Mn and Fe orbital to form a covalent bond, which is in line with previous research results. The iso-surfaces of $\Delta = \rho[LiMnPO_4] - \rho[MnPO_4]$ and $\Delta = \rho[LiMn_{3/4}Fe_{1/4}PO_4] - \rho[Mn_{3/4}Fe_{1/4}PO_4]$ are given on the left plane of Fig. 10(a). The shape of the iso-surface is similar to that of the $d(x^2 - y^2)$ orbitals, indicating that the missing electrons are located respectively in the Mn-$3d(x^2 - y^2)$ and Fe-$3d(x^2 - y^2)$ orbitals. Both the atomic projection state density and the charge difference density reveal that the Mn ion in $LiMnPO_4$ has a high spin d^4 configuration and a high spin t_{2g}^3 ($\uparrow$) $e_g^1(\uparrow)$ state. In addition, since the transition metal (TM) in $LiMn_{3/4}Fe_{1/4}PO_4$ is located in the center of the octahedron, it is possible to introduce the three-dimensional orbital splitting of the Mn and Fe transition metal ions into t_{2g} and e_g eigenstates; thus, there are representative transition metal $Mn(3d-t_{2g})^3$ and $(3d-e_g)^2$, $Fe(3d-t_{2g})^4$ and $(3d-e_g)^2$ states.

The mechanism of the band gap decrease is further explored by analyzing the orbital distribution of charge density difference. In $LiMnPO_4$ materials, the charge of the highest occupied molecular orbital (HOMO) comes from the hybridization between Mn ($3d-t_{2g}$) and O2p, and the lowest occupied molecular orbital (LUMO) comes from the hybridization of Mn ($3d-e_g$) and O 2p. In the case of Fe introduction, the HOMO orbital charge is mainly from TM ($3d-t_{2g}$) and the O 2p orbital contributes a little charge, whereas the LUMO orbital charge is due to TM ($3d-e_g$). The doping of Fe changes the hybridization pattern of Mn and O atoms at the original location and the distribution pattern of the electron cloud of the surrounding O atoms. In the process of de-lithiation, when part of Mn in the $LiMnPO_4$ material is replaced by Fe, Mn–O is replaced by Fe–O bond, with the introduction of Fe, the length of TM–O bond at

the transition metal (TM) position in the process of de-lithiation of the $LiMn_{3/4}Fe_{1/4}PO_4$ material is shortened and becomes more stable.

Fig. 10(b) records the cyclic voltammetry (CV) curves of the $LiMn_{3/4}Fe_{1/4}PO_4$/C cathode material at 0.3, 0.5, 0.7 and 0.9 mV s^{-1}, the tested start-stop voltages are respectively 2.5 V and 4.5 V. It is evident that the oxidation peak shifts somewhat towards high potential, the reduction peak shifts slightly towards low potential, and the peak current and area increase with increasing scanning speed. At each scan speed, the curves have good symmetry and redox peaks are evident, which further verify that this material has the best dynamic characteristics, which is in agreement with the aforementioned charge–discharge capability, cycle performance, rate performance, and impedance analysis. In addition, it is pointed out that the oxidation peak of the material appears at about 4.33 V, corresponding to the oxidation reaction of $Mn^{3+} \rightarrow Mn^{4+}$, i.e., the Li$^+$ removal process in the $LiMn_{3/4}Fe_{1/4}PO_4$ olivine structure. The reduction peak of the material appears at about 3.86 V, corresponding to the reduction reaction of $Mn^{4+} \rightarrow Mn^{3+}$, i.e., the Li$^+$ embedding process in the $LiMn_{3/4}Fe_{1/4}PO_4$ olivine structure.

To further determine the diffusion coefficient of Li$^+$ from the $LiMn_{3/4}Fe_{1/4}PO_4$/C cathode electrode, the relation between the peak current and the square root of sweep speed in its CV curve was fitted, as illustrated in Fig. 10(c). This shows that there is a good linear relationship between the peak current and the square root of scanning rate, and the value of R^2 is very close to 1, confirming that the redox reaction is controlled by diffusion in $LiMn_{3/4}Fe_{1/4}PO_4$/C materials. The diffusion coefficient of lithium ions from the positive electrode $LiMn_{3/4}Fe_{1/4}PO_4$/C can be calculated as 4.26×10^{-11} cm^2 s^{-1}, which is indicative of its excellent kinetic performance, based on eqn (5) and the slope in Fig. 10(c).

$$I_P = 2.69 \times 10^5 \cdot A \cdot C_{Li} \cdot n^{3/2} \cdot \sqrt{\lambda D_{Li^+}} \quad (5)$$

In the above equation, I_P – peak current (mA); A – surface area of the electrode surface vibrant material, $A = 0.64$ cm^2 in the current text; C_{Li} – Concentration of Li$^+$ in the material of the electrode, $C_{Li} = 0.0227$ mol cm^{-3} in the current test; γ – scanning speed (mV s^{-1}); D_{Li^+} – lithium ion diffusion coefficient (cm^2 s^{-1}); n – the quantity of electrons transferred in oxidation or reduction reactions, $n = 1$ in this experiment.

Fig. 10(d) further shows CV curves of $LiMn_{3/4}Fe_{1/4}PO_4$/C and $LiMnPO_4$/C samples with scanning speeds of 0.9 mV s^{-1}. Pure-phase $LiMnPO_4$/C materials exhibit only fuzzy oxidation peaks due to the severe polarization phenomenon. It can be seen that the $LiMn_{3/4}Fe_{1/4}PO_4$/C electrode showed significant redox peaks, with better symmetry and higher redox peaks, even at a high sweep velocity of 0.9 mV s^{-1}. The latent difference between the positive and negative peaks of $LiMn_{3/4}Fe_{1/4}PO_4$/C and $LiMnPO_4$/C electrodes is respectively 0.502 V and 0.717 V. Therefore, this indicates that the Mn to Fe ratio of 3 : 1 lithium manganese iron phosphate (LMFP) material has better cyclic reversibility than the pure phase $LiMnPO_4$ material. The intensity of the redox peak (especially the oxidation peak) of
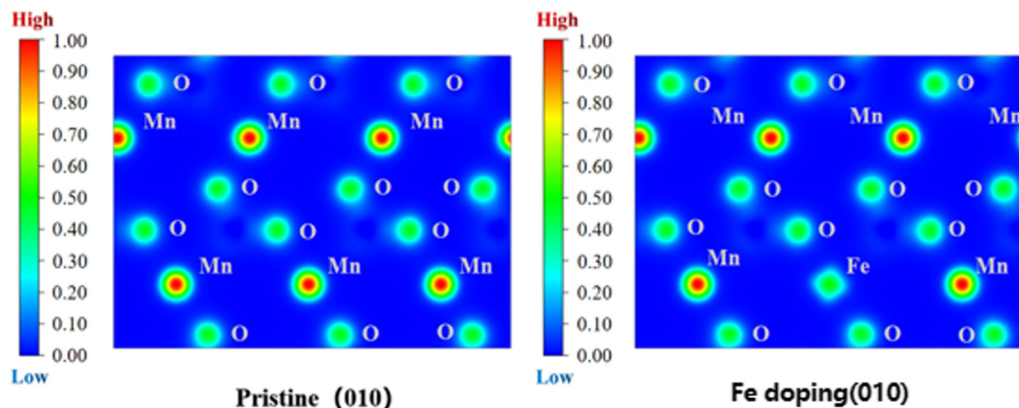
This journal is © The Royal Society of Chemistry 2024

J. Mater. Chem. C, 2024, **12**, 4961–4976 | **4973**

Fig. 11 Comparison of local charge density before and after Fe doping.

$LiMn_{3/4}Fe_{1/4}PO_4/C$ was also markedly larger than that of the pure $LiMnPO_4/C$ at the same high scanning speed of 0.9 mV s^{-1}, which dramatically reduced electrode polarization and improved reaction kinetics and chemical reaction rates. It is evident that the space enclosed by the CV curve of the $LiMn_{3/4}Fe_{1/4}PO_4/C$ material is increased, effectively enriching the specific ability of the active material.

The electron local function (ELF) is an ideal tool for describing electron distribution in space, which is very important for clarifying the properties of bonding and ion diffusion and can be used to explain the internal factors of the enhancement of lithium-ion diffusion in the CV curve. Research theory shows that the ELF value is always positive and between 0 and 1, and the closer to 0, the lower the degree of electron localization. There is little difference in the local charge between different Fe doping levels. Actually, the only things that can explain the issue in the $Li(Mn_{1-x}Fe_x)PO_4$ system are a pure phase $LiMnPO_4$ and the crystal comparison following the local doping of Fe at the same site.

Fig. 11 shows the spatial distribution of charge density of $Li(Mn_{1-x}Fe_x)PO_4$ materials; this figure shows the comparison of local charge density of $LiMnPO_4$ material along the (100) crystal plane before and after doping, revealing the charge change of the $LiMnPO_4$ crystal before and after Fe doping. In the figure, the electron density on the isosurface of electron density is 0.1 e Å^{-3}, and the redder the scale on the left, the larger the charge density, *i.e.*, "Low → High" represents "low electron density → completely delocalized electron density → completely localized electron density". Obviously, doping has a very significant effect on the charge. The localization of Fe-3d and Mn-3d electrons can be seen from the electron density profile at the doping point. After doping, the distribution range of the electron density contour in the doping site is wider than that before doping, and the electrical conductivity is better. After Fe doping, the local charge density around the original Mn site decreases, indicating that Fe atom has a stronger reducing effect on the localization of surrounding electrons than Mn. From the ELF value of doping site (Fe), it can be observed that compared with $LiMnPO_4$ of pure phase, the existence of Fe element can reduce the ELF function value near

the original Mn position; this indicates that the localization of electrons is reduced and the diffusion energy barrier is reduced, which is advantageous for electron motion and improves the diffusion rate of lithium ions in the doping system. Therefore, the more Fe content, the better, which further verified the previous conclusion that $LiMn_{3/4}Fe_{1/4}PO_4$ had the best performance.

4 Conclusion

In this paper, a high performance $Li(Mn_{1-x}Fe_x)PO_4/C$ (x = 0, 1/24, 1/12, 1/8, 1/4) positive electrode was successfully prepared through the hydrothermal method, which successfully solved the problem of poor intrinsic performance of pure phase material $LiMnPO_4$. The conclusions are as follows.

XRD, XPS and EDS tests showed that Fe elements successfully entered the $LiMnPO_4$ lattice and formed the $Li(Mn_{1-x}Fe_x)PO_4/C$ cathode material. The SEM images show that the samples are mainly spherical and attached with many small agglomeration particles. With the addition of Fe doping, the c/a value increases, indicating that doping reduces the mixing of cations; the $LiMn_{3/4}Fe_{1/4}PO_4/C$ material has the greatest c/a value. The transmission electron microscopy (TEM) images of the grains demonstrate that they are polished on the particle surface and have high crystallinity. The intrinsic quality of the high performance of the $LiMn_{3/4}Fe_{1/4}PO_4/C$ positive electrode is explained by the simulation of the electron structure and charge density. The energy difference between the highest HOMO and lowest LUMO in the total density of states (TDOS) can be used to determine the energy value near the Fermi level. This energy difference indicates that the band gaps of the $LiMn_{3/4}Fe_{1/4}PO_4/C$ material are x = 1/24, 1/12, 1/8, and 1/4, respectively, and are 3.586 eV, 3.525 eV, 3.515 eV, and 3.503 eV, which is essentially consistent with the band calculation.

Conflicts of interest

The authors declare that they have no known competing financial interests or personal relationships that could have appeared to influence the work reported in this paper.

Acknowledgements

References

1 F. Wang, J. D. Harindintwali and Z. Yuan, *et al.*, Technologies and perspectives for achieving carbon neutrality, *Innovation*, 2021, **2**(4), 100180.

2 Y. Qiu and F. Jiang, A review on passive and active strategies of enhancing the safety of lithium-ion batteries, *Int. J. Heat Mass Transfer*, 2022, **184**, 122288.

3 L. A. Román-Ramírez and J. Marco, Design of experiments applied to lithium-ion batteries: A literature review, *Appl. Energy*, 2022, **320**, 119305.

4 N. Piao, X. Gao and H. Yang, *et al.*, Challenges and development of lithium-ion batteries for low temperature environments, *ETransportation*, 2022, **11**, 100145.

5 P. U. Nzereogu, A. D. Omah and F. I. Ezema, *et al.*, Anode materials for lithium-ion batteries: A review, *Appl. Surf. Sci. Adv.*, 2022, **9**, 100233.

6 V. Aravindan, J. Gnanaraj and Y. S. Lee, *et al.*, LiMnPO$_4$–A next generation cathode material for lithium-ion batteries, *J. Mater. Chem. A*, 2013, **1**(11), 3518–3539.

7 H. Ji, G. Yang and H. Ni, *et al.*, General synthesis and morphology control of LiMnPO$_4$ nanocrystals *via* microwave-hydrothermal route, *Electrochim. Acta*, 2011, **56**(9), 3093–3100.

8 K. Zaghib, M. Trudeau and A. Guerfi, *et al.*, New advanced cathode material: LiMnPO$_4$ encapsulated with LiFePO$_4$, *J. Power Sources*, 2012, **204**, 177–181.

9 X. L. Pan, C. Y. Xu and D. Hong, *et al.*, Hydrothermal synthesis of well-dispersed LiMnPO$_4$ plates for lithium ion batteries cathode, *Electrochim. Acta*, 2013, **87**, 303–308.

10 H. Zhang, Y. Gong and J. Li, *et al.*, Selecting substituent elements for LiMnPO$_4$ cathode materials combined with density functional theory (DFT) calculations and experiments, *J. Alloys Compd.*, 2019, **793**, 360–368.

11 J. Zheng, L. Ni and Y. Lu, *et al.*, High-performance, nanostructure LiMnPO$_4$/C composites synthesized *via* one-step solid state reaction, *J. Power Sources*, 2015, **282**, 444–451.

12 J. Han, J. Yang and Z. Xu, *et al.*, Dramatic improvement in high-rate capability of LiMnPO$_4$ nanosheets *via* crystallite size regulation, *J. Alloys Compd.*, 2022, **894**, 162510.

13 J. Han, J. Yang and H. Lu, *et al.*, Effect of synthesis processes on the microstructure and electrochemical properties of LiMnPO$_4$ cathode material, *Ind. Eng. Chem. Res.*, 2022, **61**(22), 7451–7463.

14 F. A. Vásquez and J. A. Calderón, Vanadium doping of LiMnPO$_4$ cathode material: correlation between changes in the material lattice and the enhancement of the electrochemical performance, *Electrochim. Acta*, 2019, **325**, 134930.

15 V. Ragupathi, P. Panigrahi and G. S. Nagarajan, Enhanced electrochemical performance of nanopyramid-like LiMnPO$_4$/C cathode for lithium–ion batteries, *Appl. Surf. Sci.*, 2019, **495**, 143541.

16 J. Ma, Y. Li and N. S. Grundish, *et al.*, The 2021 battery technology roadmap, *J. Phys. D: Appl. Phys.*, 2021, **54**(18), 183001.

17 C. Wang, S. Li and Y. Han, *et al.*, Assembly of LiMnPO$_4$ nanoplates into microclusters as a high-performance cathode in lithium-ion batteries, *ACS Appl. Mater. Interfaces*, 2017, **9**(33), 27618–27624.

18 I. Seo, B. Senthilkumar and K. H. Kim, *et al.*, Atomic structural and electrochemical impact of Fe substitution on nano porous LiMnPO$_4$, *J. Power Sources*, 2016, **320**, 59–67.

19 H. Xu, J. Zong and F. Ding, *et al.*, Effects of Fe^{2+} ion doping on LiMnPO$_4$ nanomaterial for lithium ion batteries, *RSC Adv.*, 2016, **6**(32), 27164–27169.

20 H. Wang, Y. Yang and Y. Liang, *et al.*, LiMn$_{1-x}$Fe$_x$PO$_4$ nanorods grown on graphene sheets for ultrahigh-rate-performance lithium ion batteries, *Angew. Chem., Int. Ed.*, 2011, **123**(32), 7502–7506.

21 K. Y. Zhang, Z. Y. Gu and E. H. Ang, *et al.*, Advanced polyanionic electrode materials for potassium-ion batteries: Progresses, challenges and application prospects, *Mater. Today*, 2022, **54**, 189–201.

22 J. Z. Guo, Z. Y. Gu and M. Du, *et al.*, Emerging characterization techniques for delving polyanion-type cathode materials of sodium-ion batteries, *Mater. Today*, 2023, 221–244.

23 M. Y. Wang, X. X. Zhao and J. Z. Guo, *et al.*, Enhanced electrode kinetics and properties via anionic regulation in polyanionic Na$_{3+x}$V$_2$(PO$_4$)$_{3-x}$(P$_2$O7)x cathode material, *Green Energy Environ.*, 2022, **7**(4), 763–771.

24 Z. Y. Gu, Y. L. Heng and J. Z. Guo, *et al.*, Nano self-assembly of fluorophosphate cathode induced by surface energy evolution towards high-rate and stable sodium-ion batteries, *Nano Res.*, 2023, **16**(1), 439–448.

25 N. H. Kwon, H. Yin and T. Vavrova, *et al.*, Nanoparticle shapes of LiMnPO$_4$, Li$^+$ diffusion orientation and diffusion

This journal is © The Royal Society of Chemistry 2024

J. Mater. Chem. C, 2024, **12**, 4961–4976 | **4975**

coefficients for high volumetric energy Li^+ ion cathodes, *J. Power Sources*, 2017, **342**, 231–240.

26 C. A. Marianetti, D. Morgan and G. Ceder, First-principles investigation of the cooperative Jahn-Teller effect for octahedrally coordinated transition-metal ions, *Phys. Rev. B: Condens. Matter Mater. Phys.*, 2001, **63**(22), 224304.

27 A. Mukhopadhyay and B. W. Sheldon, Deformation and stress in electrode materials for Li-ion batteries, *Prog. Mater. Sci.*, 2014, **63**, 58–116.

28 F. Cheng, H. Wang and Z. Zhu, *et al.*, Porous $LiMn_2O_4$ nanorods with durable high-rate capability for rechargeable Li-ion batteries, *Energy Environ. Sci.*, 2011, **4**(9), 3668–3675.

29 S. Liu, L. Xiong and C. He, Long cycle life lithium ion battery with lithium nickel cobalt manganese oxide (NCM) cathode, *J. Power Sources*, 2014, **261**, 285–291.

30 Q. Zhang, C. Yan and Y. Meng, *et al.*, Hierarchical mesoporous Li_2FeSiO_4/C sheaf-rods as a high-performance lithium-ion battery cathode, *J. Alloys Compd.*, 2018, **767**, 195–203.

31 L. Li, E. Han and C. Mi, *et al.*, The effect of Ni or Pb substitution on the electrochemical performance of Li_2FeSiO_4/C cathode materials, *Solid State Ionics*, 2019, **330**, 24–32.

32 C. M. Doherty, R. A. Caruso and B. M. Smarsly, *et al.*, Hierarchically porous monolithic $LiFePO_4$/carbon composite electrode materials for high power lithium ion batteries, *Chem. Mater.*, 2009, **21**(21), 5300–5306.

33 W. Zheng, X. Huang and Y. Ren, *et al.*, Porous spherical $Na_3V_2(PO_4)_3$/C composites synthesized via a spray drying-assisted process with high-rate performance as cathode materials for sodium-ion batteries, *Solid State Ionics*, 2017, **308**, 161–166.

34 S. K. Martha, J. Nanda and G. M. Veith, *et al.*, Electrochemical and rate performance study of high-voltage lithium-rich composition: $Li_{1.2}Mn_{0.525}Ni_{0.175}Co_{0.1}O_2$, *J. Power Sources*, 2012, **199**, 220–226.

35 H. Gao, L. Wang and Y. Zhang, *et al.*, Tartaric acid assisted synthesis of Li_2FeSiO_4/C: Effect of carbon content on the electrochemical performance of Li_2FeSiO_4/C for lithium ion batteries, *Powder Technol.*, 2014, **253**, 638–643.

36 P. Gao, C. Zhang and G. Wen, Equivalent circuit model analysis on electrochemical impedance spectroscopy of lithium metal batteries, *J. Power Sources*, 2015, **294**, 67–74.

37 X. Z. Liao, Z. F. Ma and Q. Gong, *et al.*, Low-temperature performance of $LiFePO_4$/C cathode in a quaternary carbonate-based electrolyte, *Electrochem. Commun.*, 2008, **10**(5), 691–694.

38 C. Hwang, T. Kim and J. Shim, *et al.*, Fast ultrasound-assisted synthesis of Li_2MnSiO_4 nanoparticles for a lithium-ion battery, *J. Power Sources*, 2015, **294**, 522–529.